ACS APPLIED MATERIALS & INTERFACES

Research Article

www.acsami.org

TiO_2 Nanotube Array Photoelectrocatalyst and Ni–Sb–SnO_2 Electrocatalyst Bifacial Electrodes: A New Type of Bifunctional Hybrid Platform for Water Treatment

So Young Yang,[†] Wonyong Choi,[‡] and Hyunwoong Park*,[†]

[†]School of Energy Engineering, Kyungpook National University, Daegu 702-701, Korea

[‡]School of Environmental Science and Engineering, POSTECH, Pohang 790-784, Korea

Supporting Information

ABSTRACT: Bifunctional hybrid electrodes capable of generating various reactive oxygen species (ROS) over a wide range of potentials were developed by coupling electrocatalysts and photoelectrocatalysts. To achieve this, Ni-doped Sb-SnO_2 (NSS) was deposited on one side of a titanium (Ti) foil while the other side was anodized to grow a TiO_2 nanotube array (TNA) for electrochemical ozone generation and photoelectrochemical hydroxyl radical generation, respectively. Surface characterization indicated that NSS and TNA were formed and spatially separated yet electrically connected through the Ti substrate. While each catalyst possessed unique electrochemical properties, the coupling of both catalysts resulted in mixed electrochemical properties that drove electrocatalysis at high potentials and photoelectrocatalysis at low potentials. The performance of the NSS/TNA electrode for phenol decomposition was ~3 times greater than that of single-layer catalysts and ~1.5 times greater than the combined catalytic performances of the individual NSS and TNA catalysts. This synergistic effect was attributed partly to the simultaneous generation of hydroxyl radicals and ozone, followed by the production of other ROS. A mechanism for the generation of ROS was discussed.

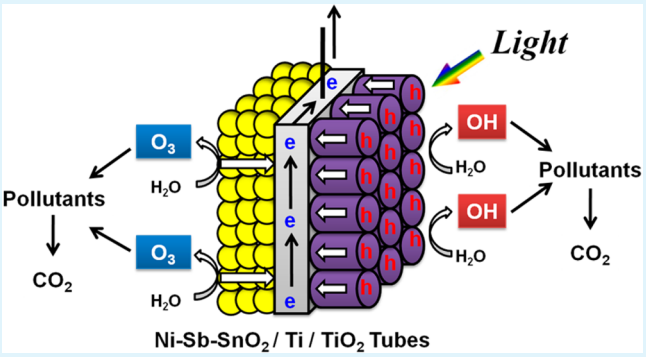

KEYWORDS: *ozone, hydroxyl radicals, synergistic, reactive oxygen species, advanced oxidation processes*

INTRODUCTION

The efficient generation of reactive oxygen species (ROS) with low energy input is crucial for the high-performance catalysis required for water treatment.[1−5] Several electrocatalysts developed for water treatment (e.g., low-oxygen evolution potential anodes) operate ~0.2 V above the water oxidation potential (R1).[1,4−11] Despite this low-potential requirement, the faradaic efficiency for the generation of ROS (R2 and R3) is not sufficiently high because of competing oxygen evolution reaction R1.[12] Therefore, increasing the applied potential does not necessarily enhance the water treatment kinetics.[13] In contrast, the faradaic efficiencies and energy consumptions of high-oxygen evolution potential anodes for the decomposition of organic species are ~7 times higher[1,11,14] and ~5 times lower,[11,14] respectively, than those of low-oxygen evolution potential anodes, presumably because of the efficient generation of OH radicals (R2).[15−19] Also, ozone can be efficiently generated (R3) instead of OH radicals by doping and modifying the base electrodes.[12,20]

$$2H_2O \rightarrow O_2 + 4e^- + 4H^+;\ E^\circ = 1.23\ V_{NHE} \quad (R1)$$

$$H_2O \rightarrow OH + e^- + H^+;\ E^\circ = 2.7\ V_{NHE} \quad (R2)$$

$$3H_2O \rightarrow O_3 + 6e^- + 6H^+;\ E^\circ = 1.51\ V_{NHE} \quad (R3)$$

However, the large potential requirement (i.e., large power input) of these electrodes increases the operating costs,[21] which offsets the high faradaic efficiency for the generation of ROS.

Alternatively, semiconductor electrodes can be considered because of their ability to photoelectrocatalytically generate OH radicals even at low potential biases (<1 V) under irradiation.[22] However, increasing the anodic potential bias does not result in a linear increase in photocurrent (i.e., the rate of ROS generation) because of the absence of the band-bending effect above a certain potential.[23,24] Under these conditions, the kinetics are limited by the incident photon flux (i.e., light intensity). Heavy doping of metal ions can increase the conductivity of semiconductors,[25] resulting in the generation of a higher current at the same potential bias. However, the semiconductors usually degenerate and permanently lose their photoelectrocatalytic abilities.

With this in mind, we attempted to design a single hybrid anode capable of generating various ROS at a variety of potentials

Received: November 3, 2014
Accepted: January 5, 2015
Published: January 5, 2015

DOI: 10.1021/am5076748
ACS Appl. Mater. Interfaces 2015, 7, 1907−1914

by coupling electrocatalysts and photoelectrocatalysts. A number of electrocatalyst and photoelectrocatalyst combinations are possible; however, a suitable match requires the generation of different ROS at both catalysts. If the same type of ROS is generated, quantitative evaluation of the performance of each catalyst becomes difficult. Ni-doped Sb-SnO_2 (NSS) electrocatalysts were selected as a candidate for ozone production because of their high faradaic efficiency even at circum-neutral pH values in various electrolytes,[12,20,26,27] while TiO_2 nanotube arrays (TNA) were selected for the generation of OH radicals because of their easy fabrication via a well-known anodization process.[23,24]

Strategic coupling of NSS and TNA is necessary for maintaining their unique functions while allowing them to operate synergistically at various potentials. In this study, the direct deposition of NSS onto the TNA surface was avoided because NSS particles would fill the pores of the TiO_2 nanotubes and potentially cover the surface, thereby decreasing the photoelectrocatalytic performance of the TNA.[23] Furthermore, large NSS loading could degenerate TiO_2, causing it to become photoinactive. Instead, NSS was deposited onto one side of a Ti foil, and the other side of the Ti foil was anodized to grow TNA. In this bifacial electrode, NSS and TNA are spatially separated yet electrically connected through the Ti substrate (Scheme 1).

Scheme 1. Illustration of Light-Assisted Electrocatalysis Using Ni-Sb-SnO_2 (NSS) Electrocatalyst and TiO_2 Nanotube Array (TNA) Photoelectrocatalyst Bifacial Electrodes[a]

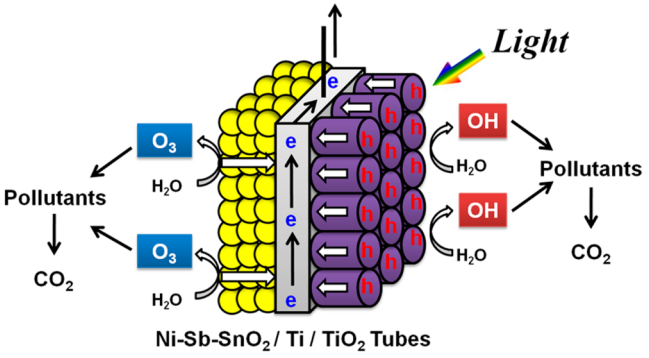

[a]OH radicals were also generated at the NSS but are not shown for the sake of simplicity.

This configuration of bifacial electrode has often been utilized in photoelectrochemical conversion systems[28−30] and for water treatments.[31] The as-fabricated NSS/TNA bifacial electrodes simultaneously generate ozone and OH radicals, and their performance in the decomposition of aqueous substrates at various potentials is superior to those of single TNA and NSS electrodes.

EXPERIMENTAL SECTION

Electrode Preparation and Surface Characterization. A Ti metal sheet (0.127 mm thick, 99.7% pure, Aldrich) was cut into small foils (1.5 cm × 4 cm), which were polished with sand paper (400-grit), ultrasonically treated in isopropyl alcohol, and washed with distilled water. One side of the pretreated foils was coupled with stainless steel and electrochemically anodized in aqueous solutions of H_3PO_4 (0.5 M, Aldrich) and NaF (0.14 M, Aldrich) for 4 h at a dc voltage of 20 V. They were then washed several times with water and annealed at 500 °C for 6 h in atmospheric air. The as-fabricated TNA showed photoconversion efficiency [i.e., incident photon-to-current efficiency value of ∼20% at λ = 340 nm (Figure S1 of the Supporting Information)][23,24] comparable to those in the literature,[32] indicating that the TNA worked properly. To generate the bifacial electrode, the other side of the foils (i.e., the side free of TNA) was carefully polished again to remove any TiO_2 created during annealing. An aliquot (0.2 mL) of a mixed solution (pH ∼0.83) of Sn^{4+} ($SnCl_4{\cdot}5H_2O$, 98%, Aldrich) in 2-propanol (Aldrich), Sb^{3+} ($SbCl_3$, 99%, Aldrich) in 2-propanol, and Ni^{2+} ($NiCl_2{\cdot}6H_2O$, more than reagent grade, Aldrich) in 1 M HCl (Aldrich) (each at 0.1 M) with a molar ratio of 95:5:1 was then added dropwise onto the repolished side and spread for 10 s at a rate of 1000 rpm using a spin-coater (JS-301-100). This procedure was repeated five times, followed by calcination at 500 °C for 5 min under atmospheric air to create the NSS film. To generate a thick NSS film, the cycle described above was repeated 10 times. Finally, robust films were produced by annealing the bifacial electrodes at 500 °C for 1 h under atmospheric air. For comparison, the same procedure was used to fabricate electrodes with either only TNA or only NSS.

The morphologies and elemental compositions of the as-prepared samples were examined by ultra-high-resolution field emission scanning electron microscopy (UHR-FE-SEM; Hitachi S-5500, resolution of 0.4 nm) operating at 30 kV. X-ray diffraction (XRD) was performed using Rigaku D/Max-2500 with Cu Kα radiation and a Ni filter. X-ray photoelectron spectroscopy (XPS) was performed using VG scientific (ESCA LAB 220i XL, Mg Kα source). XPS survey spectra for all the samples were obtained in the 0−1400 eV range to determine their elemental compositions (Table S1 of the Supporting Information). Individual element scans were also conducted for C 1s (274−294 eV), O 1s (525−545 eV), Sn 3d (480−500 eV), Sb 3d (528−549 eV), Ni (844−874 eV), and Ti 2p (451−476 eV). A Sb $3d_{5/2}$ and O 1s mixed XPS band at ∼531 eV was deconvoluted, using PeakFix (version 4), for separating and extracting the contributions of the two elements. For resolving the band, a Gaussian band centered at ∼530.5 eV (corresponding to Sb $3d_{5/2}$) was created with a given band area ratio (1.44) with respect to the Sb $3d_{3/2}$ (∼540 eV) band.[33] The area ratio of the two Sb 3d bands is constant in the XPS spectra. Then, an O 1s band was added to the 531 eV band and slightly modulated to fit between the original and simulated bands (R^2 > 0.99).

Electrochemical Study and Solution Analysis. The electrochemical and photoelectrochemical properties of the as-fabricated electrodes were analyzed by linear sweep voltammetry using a potentiostat/galvanostat (Versastat 3-400, Princeton Applied Research). A sample electrode (working electrode, 4.5 cm^2), saturated calomel electrode (SCE; reference electrode), and porous graphite rod (counter electrode) were placed in aqueous sodium sulfate solutions (0.1 M, pH ∼6), and the potentials were swept at a scan rate of 0.1 V s^{-1} from −0.5 to 2.0 V versus SCE in the absence and presence of light. Unless otherwise noted, all potential values are reported with respect to SCE. For the (photo)electrocatalytic activity tests, a constant potential (1, 1.25, and 2 V) was applied to the working electrodes in aqueous sodium sulfate solutions (0.1 M, 40 mL) without or with phenol (0.025 and 0.1 mM). The TNA sides of the electrodes were irradiated with simulated air mass (AM) 1.5 light (400 mW cm^{-2}) from a 150 W xenon arc lamp (ABET Technology), while the NSS sides faced the SCE. The simulated light power was calibrated using a standard mono-Si solar cell (K801S-K0009, McSciecne).

Phenol and its intermediates were quantified using high-performance liquid chromatography (HPLC, YL9100) with a C18 column (Thermo) at λ = 213 nm. The HPLC eluent comprised 55 vol % distilled water (including 0.1 vol % phosphoric acid) and 45 vol % acetonitrile at a flow rate of 0.5 mL min^{-1}. For quantification, standard curve fits (R^2 > 0.99) for mixed standard solutions of phenol, catechol, hydroquinone, and resorcinol were obtained using HPLC. A total organic carbon (TOC) analyzer (Teledyne Tekmar, Torch) was used to assess the degree of mineralization of phenol.

The amounts of ozone (O_3), OH radicals, and hydrogen peroxide (H_2O_2) in the aqueous phases were quantified by colorimetric methods using a UV−vis absorption spectrophotometer (PerkinElmer, Lambda 950). The ozone concentrations were determined using the indigo method, which is based on the quantitative decolorization (λ = 600 nm) of potassium indigo trisulfonate (Aldrich) that occurs upon reaction with ozone.[34] The OH radicals were estimated at λ = 440 nm using *N,N*-

DOI: 10.1021/am5076748
ACS Appl. Mater. Interfaces 2015, 7, 1907−1914

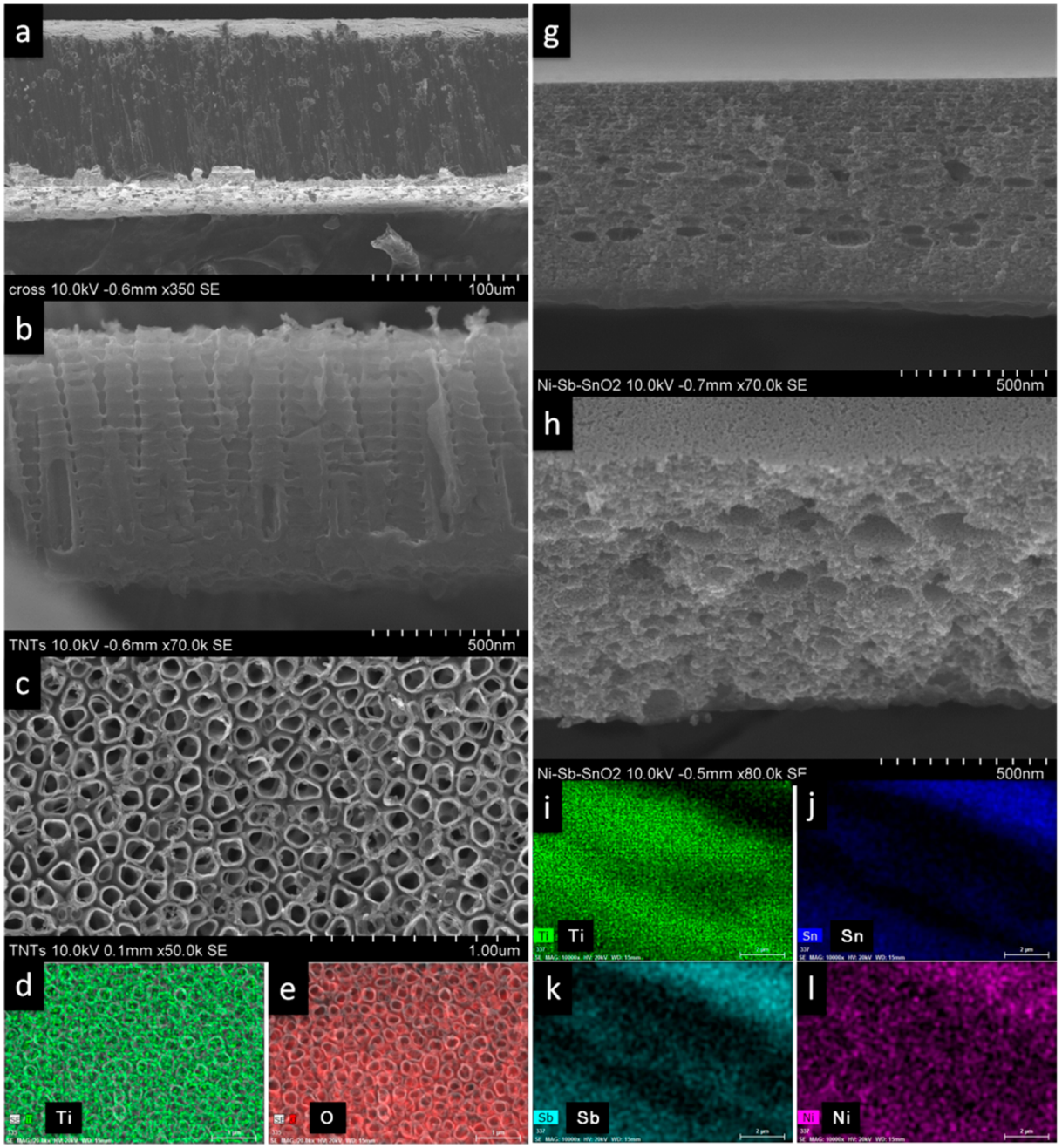

Figure 1. SEM (a–c, g, and h) and EDX (d and e for TNA and i–l for NSS) images of the NSS/TNA bifacial electrodes. (a) Cross-sectional view of NSS/TNA (top, TNA; bottom, NSS), (b and c) cross-sectional and top views of the TNA layer, and (g and h) cross-sectional views of the NSS layer (h, tilted).

dimethyl-4-nitrosoaniline (RNO, Aldrich, 25 and 50 μM) as a quencher.[35] The formation of hydrogen peroxide was determined using the 2,9-dimethyl-1,10-phenanthroline (DMP) method (λ = 454 nm) with copper(II) ions ($CuSO_4 \cdot 5H_2O$, Aldrich) and DMP (Aldrich).[36]

RESULTS AND DISCUSSION

Characterization of Electrodes. Figure 1 shows the SEM images and EDX elemental maps of the NSS/TNA bifacial electrodes. Although the sample was not smoothly cut (Figure 1a), it is obvious that both catalyst layers were formed on the same Ti substrate. A magnified view of the TNA layer shows well-formed ~800 nm long tubular bundles that were oriented vertically on the Ti substrate (Figure 1b). Each tube had a nodelike bamboo-type skeleton, which is typical of anodized TiO_2 tube arrays.[23,24,37] The diameter and mouth-wall thickness of each tube were ~10 and ~100 nm, respectively (Figure 1c). Elemental mapping revealed that the tubes were composed of Ti and O (panels d and e of Figure 1, respectively). The cross-sectional view of the NSS layer was quite different from that of the TNA layer. The NSS particles were packed into a ~750 nm thick sponge-type film containing layer-by-layer oval pores (Figure 1g and h; see Figure S2 of the Supporting Information for a top-view image). This multilayer configuration with horizontal oval pores seems to have been created during the repeated spin-coating of the NSS precursor solutions in air. Elemental mapping further verified that the NSS layer was composed of Ti, Sn, Sb,

DOI: 10.1021/am5076748
ACS Appl. Mater. Interfaces 2015, 7, 1907–1914

and Ni (Figure 1i–l, respectively) and the O:Ti and Sn:Sb:Ni atomic ratios were 1.77:1 and 20.4:1.15:1 (Table S1 of the Supporting Information), respectively. It worth noting that EDX elemental mapping scans only the spatial surface regions and does not provide information regarding elemental composition in the vertical region. Accordingly, the elemental composition obtained by analysis may be different from that of the prepared dropping solution.

Figure 2a shows the XRD patterns of an NSS/TNA sample. The TNA layer was composed of anatase and rutile phases with

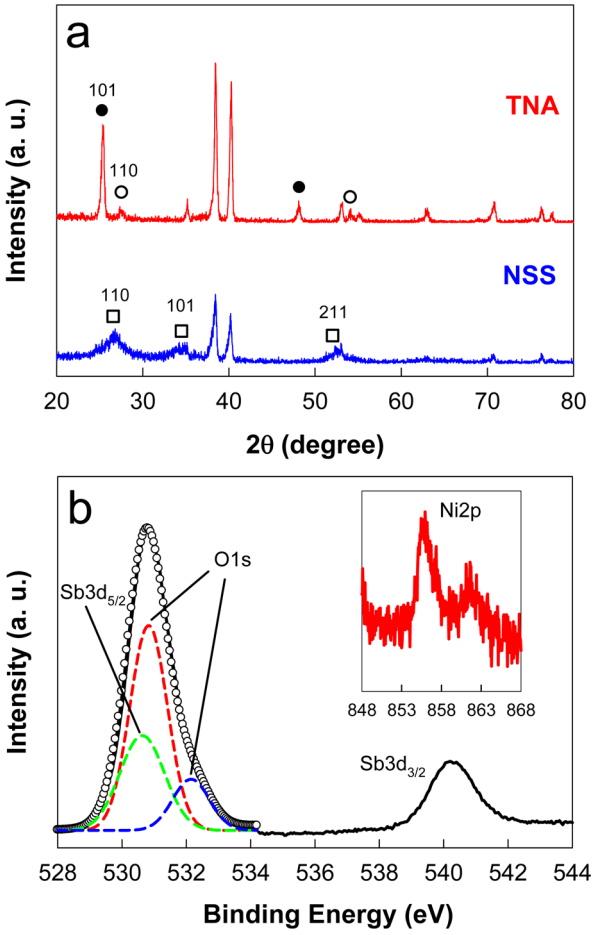

Figure 2. (a) XRD patterns of the TNA and NSS layers of the NSS/TNA bifacial electrodes: (□) SnO_2, (●) anatase TiO_2, and (○) rutile TiO_2. Unassigned peaks originate from Ti metal. (b) XPS spectra of Sb 3d and Ni 2p (inset) of the NSS layer. The band at ~530.9 eV was resolved into the Sb $3d_{5/2}$ and O 1s bands.

an overall O:Ti atomic ratio of 2.53. Although the former phase was dominant, annealing at 500 °C induced the transformation of anatase to the rutile crystalline form (JCPDS Card nos. 00-044-1294, 01-075-2552, and 01-075-6234).[32] On the other hand, the NSS layer exhibited only SnO_2-originated peaks (2θ = 26°, 34°, and 52.2°; JCPDS Card nos. 01-089-5009 and 01-072-1147); no other peaks related to Sb and Ni were found because of their low doping levels.[20] Figure 2b shows the XPS spectra of the Sb 3d and Ni 2p (inset) bands in the NSS layer. The binding energy of Sb $3d_{3/2}$ at 540.4 eV indicated the pentavalency of the doped Sb,[38] whereas the low-binding energy band at 530.8 eV was difficult to assign because of mixing of the Sb $3d_{5/2}$ and O 1s bands. Resolving the band revealed the presence of a Sb^V $3d_{5/2}$ band (530.7 eV) and two O 1s bands (530.9 and 532.2 eV); these O 1s bands are associated with metallic oxides (i.e., lattice oxygen such as SnO_2) and hydroxides (i.e., surface oxygen such as Sn-OH or hydrated species), respectively. The latter appears to actively participate in electrochemical reactions. In the NSS layer, Sn was determined to be tetravalent (e.g., SnO_2) (Figure S3 of the Supporting Information). The Sn:Sb:Ni atomic ratio was 21.9:2.6:1, which is similar to the results obtained by elemental mapping analysis (Table S1 of the Supporting Information).

Electrochemical Properties and Activities of the NSS/TNA Electrodes. Figure 3a shows the linear sweep voltammo-

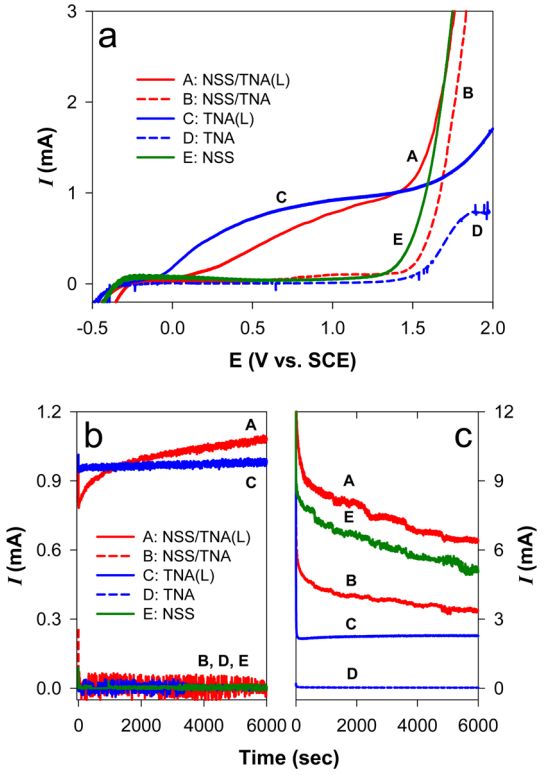

Figure 3. Electrochemical and photoelectrochemical characterization of sample electrodes in 0.1 M sodium sulfate. (a) Linear sweep voltammograms obtained at a scan rate of 0.1 V s^{-1}. (b and c) Time profiles of current generation at E = 1.0 and 2.0 V, respectively. Air-equilibrated; AM 1.5. L refers to irradiation. Note that the scale of the current (I) is different for panels b and c.

grams of the NSS, TNA, and NSS/TNA electrodes in 0.1 M sodium sulfate in the dark and under irradiation (denoted as L). The NSS electrode did not show any current generation up to an onset potential (E_{on}) of ~1.3 V but displayed a large anodic current upon reaching that potential. Accordingly, the NSS electrode should be inert for ROS generation and water treatment at low potential biases (E) and may become effective when $E > E_{on}$ (panels b and c of Figure 3, respectively). In contrast, the TNA electrodes did not generate current up to an E_{on} of ~1.5 V because of the absence of free charge carriers (Figure 3a and b); the slight increase in the current above 1.5 V was attributed to the degeneration of TiO_2 because of the shift in the Fermi level (E_F) close to the valence band edge.[39] Upon irradiation, a negative shift of the onset potential to −0.1 V was observed because of the photogeneration of charge carriers. The photocurrent increased up to ~0.95 mA with an increase in E because of the downward shift of E_F and band bending (Figure S4 of the Supporting Information). As E became greater than 1 V,

DOI: 10.1021/am5076748
ACS Appl. Mater. Interfaces 2015, 7, 1907–1914

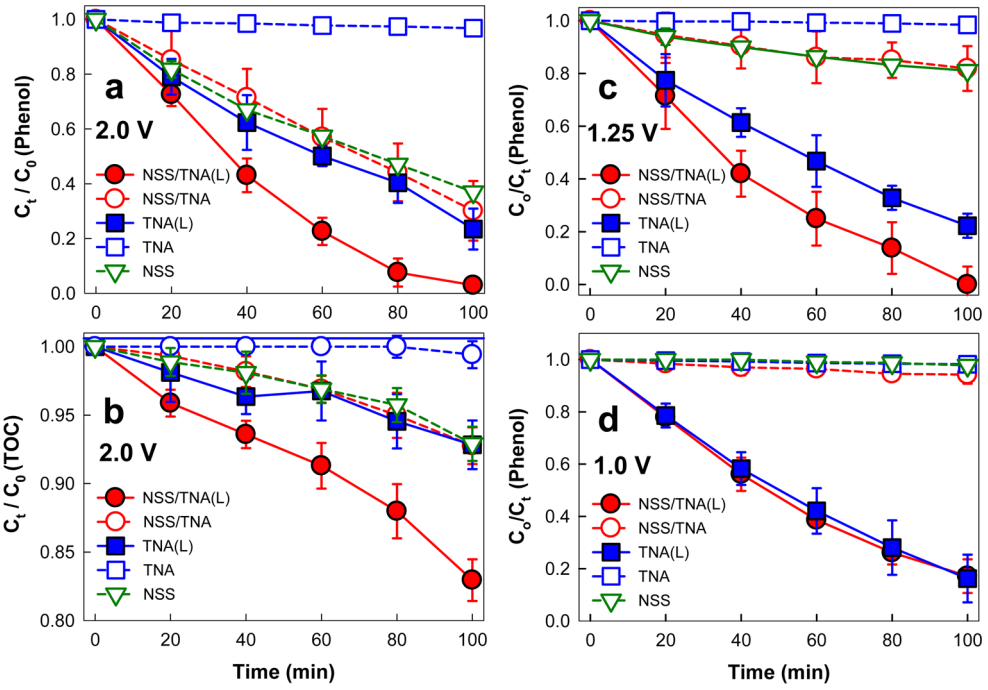

Figure 4. Time-profiled changes of (a, c, and d) phenol concentration and (b) TOC at E = 2.0 V (a and b), 1.25 V (c), and 1.0 V (d) with sample electrodes in 0.1 M sodium sulfate. $[\text{Phenol}]_0$ = 100 μM (a and b) or 25 μM (c and d). Air-equilibrated; AM 1.5. L refers to irradiation.

the band-bending effect, in terms of charge separation, decreased and the overall photoeffect was limited by the incident photon flux and charge generation in the range of 1−1.5 V. At excess bias (i.e., E > 1.5 V), E_F became close to or more positive than the valence band level, and consequently, degeneration occurred.

The behavior of the bifacial electrode (NSS/TNA) is unique. In the absence of light, it showed NSS-like behavior and its E_{on} was halfway between those of NSS and TNA; at the same potential bias, the bifacial electrode generated currents lower than that of NSS (Figure 3c) because of the positive shift of the E_{on} by ∼0.1 V (Figure 3a). Upon irradiation, the I−E shape of the bifacial electrode [NSS/TNA(L)] became similar to those of the TNA(L) and NSS electrodes in the low- and high-potential regions, respectively. This indicates that the NSS/TNA(L) electrodes possess both metallic (conductive) and semimetallic (semiconductive) character and either of the two dominates, depending on the applied potential bias. This chameleon-like behavior was further confirmed by the similar levels of current generation between TNA(L) and NSS/TNA(L) at 1.0 V (Figure 3b), and NSS and NSS/TNA(L) at 2.0 V (Figure 3c). At 2.0 V, the decrease in current generation with time for electrodes containing the NSS layer is attributed to the mass-transfer limitation.

Figure 4a shows the changes in phenol concentration with time at E = 2.0 V for various electrodes in 0.1 M sodium sulfate. For the TNA electrode, no measurable phenol degradation occurred in the dark, whereas irradiation resulted in the rapid degradation of phenol via a pseudo-first-order reaction [$C_t/C_0 = \exp(-k_{app}t)$] with a rate constant ($k_{app}$) of 1.4×10^{-2} min^{-1}. NSS displayed similar degradation kinetics [$k_{app} = 1.0 \times 10^{-2}$ min^{-1} (see Figure 5)]. At this high potential, because of the electrocatalytic properties of NSS, the degradation kinetics of NSS/TNA were comparable ($k_{app} = 1.2 \times 10^{-2}$ min^{-1}). However, the kinetics were significantly enhanced ($k_{app} = 3.6 \times 10^{-2}$ min^{-1}) upon irradiation, which was attributed to the enhanced current generation (Figure S5a of the Supporting Information) and

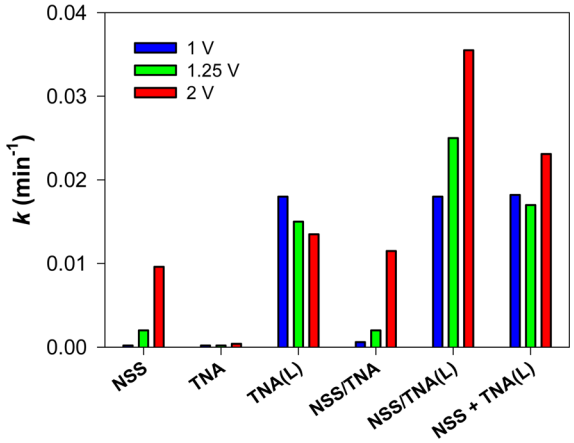

Figure 5. Comparison of the pseudo-first-order reaction rate constants (k_{app}) for phenol degradation with the sample electrodes at various potentials (1, 1.25, and 2 V) in a 0.1 M sodium sulfate electrolyte. Note that the initial concentrations of phenol were 25 μM at 1 and 1.25 V and 100 μM at 2 V. L refers to irradiation (on the TNA side), and + denotes the sum of the individual rate constants for NSS and TNA(L).

simultaneous electrocatalytic and photoelectrocatalytic reactions in the NSS/TNA(L) electrode. It is noteworthy that the rate constant of NSS/TNA(L) was 1.5 times higher than the sum of those of individual NSS and TNA(L) electrodes [1.5 = 3.6/(1.0 + 1.4)], indicating that a synergistic reaction occurs (Figure 5). Nevertheless, the current efficiency of NSS/TNA and NSS/TNA(L) for the one-electron oxidation of phenol was similar (<10%), because of enhanced current generation in the latter electrode (Figure S5a of the Supporting Information). During the degradation of phenol, hydroquinone and catechol were the primary intermediates for all the electrodes except for the TNA electrode (Figure S6 of the Supporting Information). These intermediates can interfere with phenol oxidation, reducing the current efficiency for the one-electron oxidation of phenol. The

DOI: 10.1021/am5076748
ACS Appl. Mater. Interfaces 2015, 7, 1907−1914

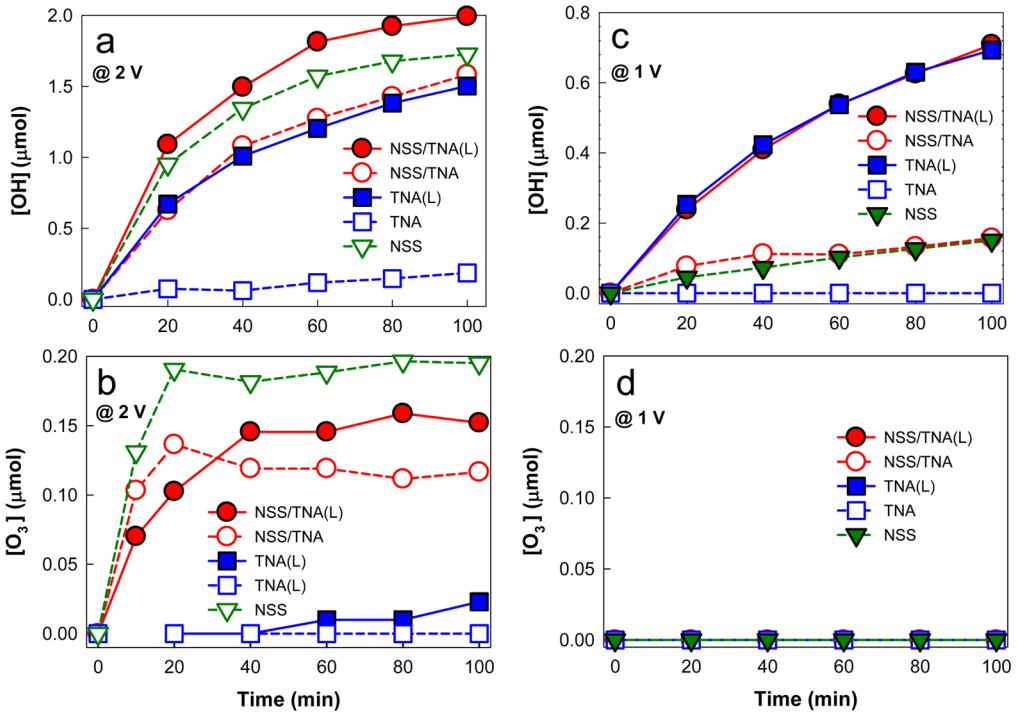

Figure 6. Time-profiled production of (a and c) OH radicals and (b and d) ozone at E = 2.0 V (a and b) and 1.0 V (c and d) for the sample electrodes in 0.1 M sodium sulfate. Air-equilibrated; AM 1.5. L refers to irradiation.

superior activity of NSS/TNA(L) was further confirmed by the change in TOC, which was 2 times greater than those obtained using NSS and TNA(L) individually (Figure 4b). Comparison of the intermediate profiles and TOC changes (Figure S6 of the Supporting Information vs Figure 4b) suggests that a significant fraction of hydroquinone and catechol degraded in the presence of NSS/TNA(L).

As the potential bias decreased, NSS, TNA, and NSS/TNA became inactive with respect to phenol degradation (Figure 4c and d). At 1.25 V, NSS was still electrocatalytically active; however, it became completely inactive at 1.0 V (Figure S5b of the Supporting Information). The latter potential was >0.3 V of the E_{on} of NSS (Figure 3a), and TNA was inactive in the absence of irradiation. Accordingly, NSS/TNA was also inactive at 1.0 V (Figure S5c of the Supporting Information). It is noteworthy that, at 1.25 V, the activity of NSS/TNA(L) was 1.7 times higher than that of TNA(L) (k_{app} = 2.5 × 10^{-2} and 1.5 × 10^{-2} min^{-1}, respectively); however, at 2.0 V, this difference decreased (Figure 5). At 1.0 V, both activities became equivalent in terms of kinetics (k_{app} = 6 × 10^{-3} min^{-1}) and TOC changes (Figure S7 of the Supporting Information), which suggests that the TNA(L) layer did not lose its activity at this potential and the NSS layer did not negatively affect the charge separation and/or transfer occurring at the TNA(L) layer.

Photoelectrocatalytic ROS Generation and Reactions. The unique catalytic properties of the bifacial electrodes were further examined and compared, in terms of ROS generation, to those of other electrodes (Figure 6). At E = 2.0 V, for the NSS/TNA(L) electrode, the level of production of OH radicals increased exponentially and reached a plateau at 2 μmol after electrolysis for 1 h under irradiation (Figure 6a). This amount was greater than those obtained using NSS (1.7 μmol), NSS/TNA (1.6 μmol), and TNA(L) (1.5 μmol). The fact that the level of production of OH radicals was the highest for NSS/TNA(L) was consistent with the fact that its current generation was also the highest (Figure 3c). This resulted in similar current efficiencies (~2%) for NSS/TNA(L) and NSS/TNA. This is reasonable because OH radicals, which are a typical initial product during the electrolysis of aqueous media, were simultaneously generated on both catalysts. On the other hand, the trends for ozone production were quite different from those of the production of OH radicals (Figure 6b). For example, the level of ozone production was the highest for NSS, with a current efficiency of ~1%, followed by NSS/TNA(L) and NSS/TNA. Although the latter two had the same NSS layers, NSS/TNA(L) in particular generated a current higher than that of NSS (Figure 3c). This suggests the presence of additional ozone-quenching pathways for NSS/TNA(L). Another difference is that a shorter time was required to reach the ozone generation plateau (~20 min) compared to that for the OH radicals (>60 min). This situation occurs only when the ozone-quenching rate is greater than or comparable to its production rate. Otherwise, ozone would continually accumulate, and its amount would increase gradually with time.

When OH radicals and ozone are produced simultaneously [the cases of NSS, NSS/TNA, and NSS/TNA(L) at 2 V], they can react to produce hydroperoxyl radicals (HO_2) at a bimolecular reaction rate k_4 of ~10^8 M^{-1} s^{-1} (reaction R4 and Scheme 2).[40] Subsequently, the HO_2 species are either transformed to OH radicals via a reaction with ozone (k < 10^4 M^{-1} s^{-1}), converted to hydrogen peroxide by coupling with themselves (k ~ 10^6 M^{-1} s^{-1}), or quenched by hydroxyl radicals (k_5 ~ 10^9 M^{-1} s^{-1}) (reaction R5).

$$OH^{\bullet} + O_3 \rightarrow HO_2 + O_2 \quad \text{(R4)}$$

$$OH^{\bullet} + HO_2 \rightarrow H_2O + O_2 \quad \text{(R5)}$$

The primary ozone-quenching pathways involve reactions with OH radicals as well as superoxides (O_2^-) (Scheme 2), while the reaction of ozone with a substrate (S; i.e., phenol in this

DOI: 10.1021/am5076748
ACS Appl. Mater. Interfaces 2015, 7, 1907−1914

Scheme 2. Primary Elementary Reaction Pathways of the Reactive Oxygen Species Generated at the NSS/TNA Bifacial Electrodes[a]

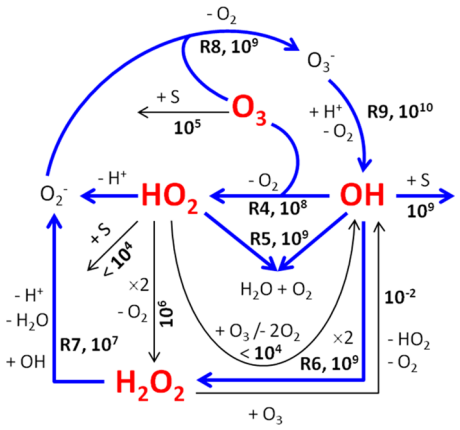

[a]Reactions R1−R3 are given in the text, and the approximate bimolecular reaction rate constants (k, liters per mole per second) are shown with the corresponding reactions. S refers to phenol.

study) is relatively slow ($k \sim 10^5$ M^{-1} s^{-1}).[41] On the other hand, most OH radical-quenching rates are diffusion-limited ($k > 10^9$ M^{-1} s^{-1})[42] and the OH radicals are partially replenished by reactions among HO_2, O_3, and H_2O_2. This replenishing pathway shifts the balance between (photo)electrocatalytic production and quenching, and consequently delays the saturation of OH radicals.

At 2 V, using NSS/TNA(L), a larger amount of OH radicals is generated because of the contribution of TNA(L) (Figure 6a), and hence, the R4 pathway should be facilitated; the reduced amount of ozone supports this hypothesis (Figure 6b). Although the enhanced production of OH radicals can facilitate R5, as well, the coupling of two OH radicals (i.e., H_2O_2 production, reaction R6) competitively occurs at a similar rate ($k_6 \sim 10^9$ M^{-1} s^{-1}). Continuous generation of H_2O_2 occurred with only NSS/TNA(L) (Figure S8 of the Supporting Information), further suggesting that superoxides could be generated via R7 (Scheme 2).[43] Superoxides are good quenchers of ozone with a k_8 of $\sim 10^9$ M^{-1} s^{-1} (reaction R8), which, in combination with reaction R4, further reduce the level of ozone production and lead to the production of OH radicals (reaction R9).

$$OH + OH \rightarrow H_2O_2 \quad (R6)$$

$$OH + H_2O_2 \rightarrow O_2^- + H_2O + H^+ \quad (R7)$$

$$O_2^- + O_3 \rightarrow O_3^- + O_2 \quad (R8)$$

$$O_3^- + H^+ \rightarrow OH + O_2 \quad (R9)$$

At 1.0 V, the reaction mechanism appears to be straightforward because a relatively large amount of OH radicals was found only with TNA(L) and NSS/TNA(L) (Figure 6c). It is noteworthy that the TNA(L) and NSS/TNA(L) electrodes generated the same amounts of OH radicals, which suggests that photoelectrocatalysis was the primary reaction at this potential. The equivalent changes in TOC support this conclusion (Figure S7 of the Supporting Information). The lack of ozone production in all the electrodes (Figure 6d) further supports the minor contribution of electrocatalysis.

CONCLUSIONS

This study demonstrated that TiO_2 nanotube array photoelectrocatalyst and Ni−Sb−SnO_2 electrocatalyst bifacial electrodes operate effectively for the decomposition of phenol and the generation of ROS over a wide range of electrical potentials. Each catalyst possesses unique electrochemical properties, and the coupling of these catalysts results in synergistic electrocatalytic performance without the loss of their individual electrochemical properties. In particular, the electrocatalytic performance of the bifacial electrodes is ~3 times greater than those of single-layered electrodes; moreover, it is ~1.5 times greater than even the sum of the performances of both electrodes, when they are both simultaneously operational. This synergistic effect is attributed partly to the simultaneous generation of ROS, such as hydroxyl radicals, ozone, and hydrogen peroxides, all of which contribute to the decomposition of substrates. This bifacial electrode possesses a high application potential for surface and subsurface wastewater treatment. Considering the low penetration depth of sunlight in typical wastewater, the surface and subsurface waters could be treated with TiO_2 nanotube arrays and Ni-Sb-SnO_2 electrocatalysts, respectively.

ASSOCIATED CONTENT

Supporting Information

Table S1 and Figures S1−S8. This material is available free of charge via the Internet at http://pubs.acs.org.

AUTHOR INFORMATION

Corresponding Author

*Telephone: +82-53-950-8973. Fax: +82-53-950-8979. E-mail: hwp@knu.ac.kr.

Notes

The authors declare no competing financial interest.

ACKNOWLEDGMENTS

This research was financially supported by the Basic Science Research Program (NRF-2012R1A2A2A01004517), the Global Research Network Program (NRF-2014S1A2A2027802), and the Space Core Technology Development Program (NRF-2014M1A3A3A02034875), Korea. In addition, we are grateful to the Korea CCS R&D Center (KCRC) (No. 2014M1A8A1049354) funded by the Ministry of Science, ICT, & Future Planning (MSIP). W.C. is grateful to the Global Research Laboratory Program (NRF-2014K1A1A2041044) funded by the MSIP.

REFERENCES

(1) Panizza, M.; Cerisola, G. Direct and Mediated Anodic Oxdation of Organic Pollutants. *Chem. Rev.* **2009**, *109*, 6541−6569.

(2) Feng, Y. J.; Li, X. Y. Electrocatalytic Oxidation of Phenol on Several Metal-Oxide Electrodes in Aqueous Solution. *Water Res.* **2003**, *37*, 2399−2407.

(3) Simond, O.; Schaller, V.; Comninellis, C. Theoretical Model for the Anodic Oxidation of Organics on Metal Oxide Electrodes. *Electrochim. Acta* **1997**, *42*, 2009−2012.

(4) Trasatti, S. Electrocatalysis: Understanding the Success of DSA(R). *Electrochim. Acta* **2000**, *45*, 2377−2385.

(5) Boye, B.; Dieng, M. M.; Brillas, E. Degradation of Herbicide 4-Chlorophenoxyacetic Acid by Advanced Electrochemical Oxidation Methods. *Environ. Sci. Technol.* **2002**, *36*, 3030−3035.

(6) Park, H.; Bak, A.; Ahn, Y. Y.; Choi, J.; Hoffmann, M. R. Photoelectrochemical Performance of Multi-layered BiOx-TiO_2/Ti

DOI: 10.1021/am5076748
ACS Appl. Mater. Interfaces 2015, 7, 1907−1914

Electrodes for Degradation of Phenol and Production of Molecular Hydrogen in Water. *J. Hazard. Mater.* **2012**, *211−212*, 47−54.
(7) Park, H.; Vecitis, C. D.; Choi, W.; Weres, O.; Hoffmann, M. R. Solar-Powered Production of Molecular Hydrogen from Water. *J. Phys. Chem. C* **2008**, *112*, 885−889.
(8) Park, H.; Vecitis, C. D.; Hoffmann, M. R. Solar-Powered Electrochemical Oxidation of Organic Compounds Coupled with the Cathodic Production of Molecular Hydrogen. *J. Phys. Chem. A* **2008**, *112*, 7616−7626.
(9) Park, H.; Vecitis, C. D.; Hoffmann, M. R. Electrochemical Water Splitting Coupled with Organic Compound Oxidation: The Role of Active Chlorine Species. *J. Phys. Chem. C* **2009**, *113*, 7935−7945.
(10) Kim, J.; Choi, W. J. K.; Choi, J.; Hoffmann, M. R.; Park, H. Electrolysis of Urea and Urine for Solar Hydrogen. *Catal. Today* **2013**, *199*, 2−7.
(11) Liu, H.; Vajpayee, A.; Vecitis, C. D. Bismuth-Doped Tin Oxide-Coated Carbon Nanotube Network: Improved Anode Stability and Efficiency for Flow-Through Organic Electrooxidation. *ACS Appl. Mater. Interfaces* **2013**, *5*, 10054−10066.
(12) Yang, S. Y.; Kim, D.; Park, H. Shift of the Reactive Species in the Sb-SnO_2-Electrocatalyzed Inactivation of *E. coli* and Degradation of Phenol: Effects of Nickel Doping and Electrolytes. *Environ. Sci. Technol.* **2014**, *48*, 2877−2884.
(13) Kim, J.; Kwon, D.; Kim, K.; Hoffmann, M. R. Electrochemical Production of Hydrogen Coupled with the Oxidation of Arsenite. *Environ. Sci. Technol.* **2014**, *48*, 2059−2066.
(14) Stucki, S.; Kotz, R.; Carcer, B.; Suter, W. Electrochemical Waste Water Treatment Using High Overvoltage Anodes Part II: Anode Performance and Applications. *J. Appl. Electrochem.* **1991**, *21*, 99−104.
(15) Ferro, S.; De Battisti, A.; Duo, I.; Comninellis, C.; Haenni, W.; Perret, A. Chlorine Evolution at Highly Boron-doped Diamond Electrodes. *J. Electrochem. Soc.* **2000**, *147*, 2614−2619.
(16) Montilla, F.; Morallon, E.; Vazquez, J. L. Evaluation of the Electrocatalytic Activity of Antimony-doped Tin Dioxide Anodes Toward the Oxidation of Phenol in Aqueous Solutions. *J. Electrochem. Soc.* **2005**, *152*, B421−B427.
(17) Kim, S.; Choi, S. K.; Yoon, B. Y.; Lim, S. K.; Park, H. Effects of Electrolyte on the Electrocatalytic Activities of RuO_2/Ti and Sb-SnO_2/Ti Anodes for Water Treatment. *Appl. Catal., B* **2010**, *97*, 135−141.
(18) Niu, J.; Lin, H.; Gong, C.; Sun, X. Theoretical and Experimental Insights into the Electrochemical Mineralization Mechanism of Perfluorooctanoic Acid. *Environ. Sci. Technol.* **2013**, *47*, 14341−14349.
(19) Lin, H.; Niu, J.; Ding, S.; Zhang, L. Electrochemical Degradation of Perfluorooctanoic acid (PFOA) by Ti/SnO_2-Sb, Ti/SnO_2-Sb/PbO_2 and Ti/SnO_2-Sb/MnO_2 Anodes. *Water Res.* **2012**, *46*, 2281−2289.
(20) Yang, S. Y.; Choo, Y. S.; Kim, S.; Lim, S. K.; Lee, J.; Park, H. Boosting the Electrocatalytic Activities of SnO_2 Electrodes for Remediation of Aqueous Pollutants by Doping with Various Metals. *Appl. Catal., B* **2012**, *111*, 317−325.
(21) Cho, K.; Qu, Y.; Kwon, D.; Zhang, H. H.; Cid, C. A.; Aryanfar, A.; Hoffmann, M. R. Effects of Andoic Potential and Chloride Ion on Overall Reactivity in Electrochemical Reactors Designed for Solar-Powered Wastewater Treatment. *Environ. Sci. Technol.* **2014**, *48*, 2377−2384.
(22) Park, H.; Kim, W.; Park, Y.; Choi, W. Surface Modification of TiO_2 Photocatalyst for Environmental Applications. *J. Photochem. Photobiol., C* **2013**, *15*, 1−20.
(23) Jeon, T. W.; Choi, W.; Park, H. Photoelectrochemical and Photocatalytic Behaviors of Hematite-Decorated Titania Nanotube Arrays: Energy Level Mismatch versus Surface Specific Reactivity. *J. Phys. Chem. C* **2011**, *115*, 7134−7142.
(24) Kang, U.; Park, H. Lithium Ion-Inserted TiO_2 Nanotube Array Photoelectrocatalysts. *Appl. Catal., B* **2013**, *140−141*, 233−240.
(25) Kesselman, J. M.; Weres, O.; Lewis, N. S.; Hoffmann, M. R. Electrochemical Production of Hydroxyl Radical at Polycrystalline Nb-doped TiO_2 Electrodes and Estimation of the Partitioning Between Hydroxyl Radical and Direct Hole Oxidation Pathways. *J. Phys. Chem. B* **1997**, *101*, 2637−2643.
(26) Wang, Y. H.; Cheng, S. A.; Chan, K. Y.; Li, X. Y. Electrolytic Generation of Ozone on Antimony- and Nickel-Doped Tin Oxide Electrode. *J. Electrochem. Soc.* **2005**, *152*, D197−D200.
(27) Christensen, P. A.; Lin, W. F.; Christensen, H.; Imkum, A.; Jin, J. M.; Li, G.; Dyson, C. M. Room Temperature, Electrochemical Generation of Ozone with 50% Current Efficiency in 0.5 M Sulfuric Acid at Cell Voltages < 3 V. *Ozone: Sci. Eng.* **2009**, *31*, 287−293.
(28) Liu, Z. Y.; Misra, M. Bifacial Dye-Sensitized Solar Cells Based on Vertically Oriented TiO_2 Nanotube Arrays. *Nanotechnology* **2010**, *21*, 125703.
(29) Mor, G. K.; Varghese, O. K.; Wilke, R. H. T.; Sharma, S.; Shankar, K.; Latempa, T. J.; Choi, K. S.; Grimes, C. A. p-Type Cu-Ti-O Nanotube Arrays and Their Use in Self-Biased Heterojunction Photoelectrochemical Diodes for Hydrogen Generation. *Nano Lett.* **2008**, *8*, 1906−1911.
(30) Wang, G. M.; Yang, X. Y.; Qian, F.; Zhang, J. Z.; Li, Y. Double-Sided CdS and CdSe Quantum Dot Co-Sensitized ZnO Nanowire Arrays for Photoelectrochemical Hydrogen Generation. *Nano Lett.* **2010**, *10*, 1088−1092.
(31) Asmussen, R. M.; Tian, M.; Chen, A. C. A New Approach to Wastewater Remediation Based on Bifunctional Electrodes. *Environ. Sci. Technol.* **2009**, *43*, 5100−5105.
(32) Grimes, C. A.; Mor, G. K. *TiO_2 Nanotube Arrays: Synthesis, Properties, and Applications*; Springer: New York, 2009.
(33) Montilla, F.; Morallon, E.; De Battisti, A.; Barison, S.; Daolio, S.; Vazquez, J. L. Preparation and Characterization of Antimony-Doped Tin Dioxide Electrodes. 3. XPS and SIMS Characterization. *J. Phys. Chem. B* **2004**, *108*, 15976−15981.
(34) Bader, H.; Hoigen, J. Determination of Ozone in Water by the Indigo Method. *Water Res.* **1981**, *15*, 449−456.
(35) Comninellis, C. Electrocatalysis in the Electrochemical Conversion/Combustion of Organic Pollutants for Waste-Water Treatment. *Electrochim. Acta* **1994**, *39*, 1857−1862.
(36) Kosaka, K.; Yamada, H.; Matsui, S.; Echigo, S.; Shishida, K. Comparison Among the Methods for Hydrogen Peroxide Measurements to Evaluate Advanced Oxidation Processes: Application of a Spectrophotometric Method Using Copper(II) Ion and 2,9-Dimethyl-1,10-Phenanthroline. *Environ. Sci. Technol.* **1998**, *32*, 3821−3824.
(37) Roy, P.; Berger, S.; Schmuki, P. TiO_2 Nanotubes: Synthesis and Applications. *Angew. Chem., Int. Ed.* **2011**, *50*, 2904−2939.
(38) Available at http://srdata.nist.gov/xps/main_search_menu.aspx.
(39) Finklea, H. O. *Semiconductor Electrodes*; Elsevier: Amsterdam, 1988.
(40) Bielski, B. H. J.; Cabelli, D. E.; Arudi, R. L.; Ross, A. B. Reactivity of HO_2/O_2^- Radicals in Aqueous Solution. *J. Phys. Chem. Ref. Data* **1985**, *14*, 1041−1100.
(41) Beltran, F. J. *Ozone Reaction Kinetics for Water and Wastewater Systems*; Lewis Publishers: Albany, NY, 2003.
(42) Buxton, G. V.; Greenstock, C. L.; Helman, W. P.; Ross, A. B. Critical Review of Rate Constants for Reactions of Hydrated Electrons, Hydrogen Atoms and Hydroxyl Radicals (OH/O^-) in Aqueous Solution. *J. Phys. Chem. Ref. Data* **1988**, *17*, 513−886.
(43) Christensen, H.; Sehested, K.; Corfitzen, H. Reactions of Hydroxyl Radicals with Hydrogen Peroxide at Ambient and Elevated Temperatures. *J. Phys. Chem.* **1982**, *86*, 1588−1590.

DOI: 10.1021/am5076748
ACS Appl. Mater. Interfaces 2015, 7, 1907−1914